

On the Origin of the Monoceros Ring - I: Kinematics, proper motions, and the nature of the progenitor

Magda Guglielmo¹*, Richard R. Lane^{2,3}, Blair C. Conn⁴, Anna Y. Q. Ho⁵,
Rodrigo A. Ibata⁶ and Geraint F. Lewis¹

¹*Sydney Institute for Astronomy, School of Physics, A28, The University of Sydney, NSW 2006, Australia*

²*Millennium Institute of Astrophysics, Av. Vicuña Mackenna 4860, 782-0436 Macul, Santiago, Chile*

³*Instituto de Astrofísica, Pontificia Universidad Católica de Chile, Av. Vicuña Mackenna 4860, Santiago, Chile*

⁴*Research School of Astronomy and Astrophysics, Australian National University, Canberra, ACT 2611, Australia*

⁵*Cahill Center for Astrophysics, California Institute of Technology, MC 249-17, 1200 E California Blvd, Pasadena, CA, 91125, USA*

⁶*Observatoire astronomique de Strasbourg, Université de Strasbourg, CNRS, UMR 7550, 11 rue de l'Université, F-67000 Strasbourg, France*

Accepted XXX. Received YYY; in original form ZZZ

ABSTRACT

The Monoceros Ring (MRI) structure is an apparent stellar overdensity that has been postulated to entirely encircle the Galactic plane and has been variously described as being due to line-of-sight effects of the Galactic warp and flare or of extragalactic origin (via accretion). Despite being intensely scrutinised in the literature for more than a decade, no studies to-date have been able to definitively uncover its origins. Here we use *N*-body simulations and a genetic algorithm to explore the parameter space for the initial position, orbital parameters and, for the first time, the final location of a satellite progenitor. We fit our models to the latest Pan-STARRS data to determine whether an accretion scenario is capable of producing an in-Plane ring-like structure matching the known parameters of the MRI. Our simulations produce streams that closely match the location, proper motion and kinematics of the MRI structure. However, we are not able to reproduce the mass estimates from earlier studies based on Pan-STARRS data. Furthermore, in contrast with earlier studies our best-fit models are those for progenitors on retrograde orbits. If the MRI was produced by satellite accretion, we find that its progenitor has an initial mass upper limit of $\sim 10^{10} M_{\odot}$ and the remnant is likely located behind the Galactic bulge, making it difficult to locate observationally. While our models produce realistic MRI-like structures we cannot definitively conclude that the MRI was produced by the accretion of a satellite galaxy.

Key words: Galaxy: structure, Galaxy: evolution, Galaxy: disc, Galaxy: stellar content

1 INTRODUCTION

Surveys targeting the Milky Way (MW) disc during the past decade or so have uncovered many intriguing structures in its outer regions. With each of these discoveries questions naturally arise as to their origins and, as more of these structures are uncovered, how they relate to the origin and evolution of the Disc itself.

Arguably the most intriguing of these is a stellar overdensity apparently encircling the Disc dubbed the Monoceros Ring¹ (MRI). This structure is particularly interesting because of its implications. If the MRI is of extragalactic origin then it is likely the remnants of an in-Plane accretion event, the only extant example of its type known in the Galaxy. In-plane accretion drives disc evolution by

depositing stellar and gaseous material directly onto the disc, in a similar way to how the accretion of satellites on more polar orbits deposits material into the galactic halo (as the Sagittarius dwarf galaxy, Ibata et al. 1994, does).

First uncovered (Newberg et al. 2002) as a large stellar overdensity located ~ 18 kpc from the Galactic centre and with a scale height of ~ 2 kpc and a scale length of ~ 10 kpc, the MRI has subsequently been observed from 14–18 kpc from the Galactic centre over Galactic longitudes of $60^{\circ} < l < 280^{\circ}$ and at distances from the Galactic plane of $|z| < 5$ kpc (e.g. Yanny et al. 2003; Ibata et al. 2003; Rocha-Pinto et al. 2003; Conn et al. 2005a,b, 2007, 2008, 2012; Sollima et al. 2011).

Two explanations for the origin of the MRI have dominated the literature since it was uncovered (see Morganson et al. 2016, for a detailed review of the history of studies of the MRI to-date), namely a disrupting satellite and a Galactic origin scenario. The announcement of a possible dwarf galaxy in Canis Major (Martin et al. 2004) apparently boosted the possibility of it being formed

* e-mail: magda.guglielmo@sydney.edu.au

¹ Other names for this structure in the literature include: Galactic Anticenter Stellar Stream; Galactic Anticenter Stellar Structure; Monoceros Stream; Monoceros Overdensity

by a disrupting satellite (e.g. [Helmi et al. 2003](#); [Martin et al. 2004](#); [Peñarrubia et al. 2005, 2006](#); [Martin et al. 2006](#); [Conn et al. 2007](#); [Sollima et al. 2011](#)). While in-plane accretion events could explain the origins of the MRI, it is still unclear whether the Canis Major region could host a dwarf galaxy remnant. [Mateu et al. \(2009\)](#), for example, reports that the Canis Major region has no overdensity of RR Lyrae stars as would be expected for a dwarf galaxy of this size. There is still debate over the origins of the Blue Plume stars in Canis Major ([Carraro et al. 2005](#)) and no open clusters have been definitively associated with it. This does not exclude the possibility of an in-plane accretion event but does raise concerns about Canis Major being a dwarf galaxy and the progenitor the MRI.

As for Galactic origins, line-of-sight effects of the warp and flare of the Disc (e.g. [López-Corredoira & Molgó 2014](#); [Kalberla et al. 2014](#)), and caustics in the dark matter profile of the Galaxy ([Sikivie 2003](#); [Natarajan & Sikivie 2007](#); [Duffy & Sikivie 2008](#)) have also been investigated as reasons for the apparently ring-like stellar overdensity. More recently, apparent radial waves in the Disc observed in Sloan Digital Sky Survey (SDSS: [York et al. 2000](#)) data were uncovered by [Xu et al. \(2015\)](#). These ripples may have been caused by, for example, interactions between the Galaxy and a Sagittarius-like dwarf satellite galaxy (e.g. [Younger et al. 2008](#); [Purcell et al. 2012](#); [Gómez et al. 2013](#)) and this has also been suggested as a solution to the MRI origin problem. Examination of these different scenarios reveal that the warp and flare models typically work for individual fields but generally have different parameters between fields and as such have no single solution for the entire structure. The other scenarios are either mostly qualitative or make predictions that are not seen in the data and consequently there is still no definitive explanation for the origin of the MRI.

It is also interesting to note that the rotation curve of the MW has a "kinematic dip" at ~ 9 kpc Galactocentric radius. The cause of this is unknown but a possible explanation is a massive stellar ring at this distance from the Galactic centre. The stellar ring, if it's existence can be confirmed, may be related to the Perseus spiral arm and is, therefore, likely not associated with the MRI ([Sofue et al. 2009](#)). Furthermore, the Galactocentric distance of this purported stellar ring does not match well with the distance to the MRI and we only mention it here for completeness.

Recently [Morganson et al. \(2016\)](#) analysed Pan-STARRS-1 ([Kaiser et al. 2010](#)) data to estimate the three dimensional structure and stellar mass of the MRI. The region probed by the study where the MRI is most visible in the Pan-STARRS-1 dataset was $120^\circ < l < 240^\circ$; $-30^\circ < b < +40^\circ$ and the total excess stellar mass was estimated as $4 \times 10^6 M_\odot$. However, despite the $3\pi^\circ$ sky coverage and depth ($g \sim r \lesssim 21.7$) of Pan-STARRS-1 the origins of the MRI remain unclear.

This work aims to reproduce the observed properties of the MRI. Using *N*-body simulations combined with a Genetic Algorithm, we examine the consequences of the accretion of a satellite to explore whether an overdensity of stars such as the MRI can form from such an accretion. The method enables a rigorous search of the parameter space with the selection of possible solutions by an automatic comparison between simulation results and data constraints, as described by [Guglielmo et al. \(2014\)](#) and, furthermore, allows for the current progenitor location to be estimated for the first time. In a subsequent paper we will address the rippled Disc hypothesis using similar methodology.

Parameter	Value
M_{disk}	$7.1 \times 10^{10} M_\odot$
r_{disk}	3.0 kpc
b_{disk}	0.3 kpc
M_{bulge}	$0.7 \times 10^{10} M_\odot$
r_{bulge}	2.1 kpc
M_{vir}	$1.3 \times 10^{12} M_\odot$
R_{vir}	283 kpc
c	17

Table 1. Assumed parameters for the gravitational potential of the Milky Way

2 MODEL

2.1 *N*-body Simulations

All of the simulations were carried out using the *N*-body code Gadget-2 ([Springel 2005](#)). The original code has been modified to include the Milky Way gravitational influence on the progenitor. The equation of motion is, therefore, described by:

$$\ddot{\mathbf{r}} = \frac{\partial \phi_{\text{MW}}(|\mathbf{r}|)}{\partial \mathbf{r}} + \frac{\mathbf{F}_{\text{df}}}{M_{\text{sat}}} \quad (1)$$

where ϕ_{MW} is the total Galactic potential, M_{sat} is the satellite mass and \mathbf{F}_{df} is the dynamical friction felt by the satellite when moving in the MW dark matter halo. We describe the MW as a static, three-component potential, consisting of a an exponential disk and a spherical bulge embedded into a dark matter spherical halo. The disk is modelled by a [Miyamoto & Nagai \(1975\)](#) potential, given by:

$$\phi_D(R, z) = -\frac{GM_{\text{disk}}}{\left(R^2 + (r_{\text{disk}} + \sqrt{b^2 + x^2})^2\right)^{1/2}}. \quad (2)$$

For the bulge component, we assumed a [Hernquist \(1990\)](#) profile, described by:

$$\phi_B(r) = -\frac{GM_{\text{bulge}}}{r_{\text{bulge}} + r}. \quad (3)$$

Finally, the dark mark matter halo follows a NFW profile ([Navarro et al. 1997](#)), given by:

$$\phi_H(r) = -\frac{GM_{\text{vir}}c}{R_{\text{vir}}g(c)} \ln\left(\frac{rc}{R_{\text{vir}}} + 1\right) \quad (4)$$

where c is the concentration parameter and $g(c) = \ln(c+1) - c/(c+1)$.

Table 1 summarises the parameters used for the mass and radius of each component. They are constant through all our simulations. Our choice of parameters reproduces the current MW circular velocity at the solar position ($R_\odot = 8.29$ kpc), $V_{\text{cir}} = 239 \text{ km s}^{-1}$ ([McMillan 2011](#)) and are consistent with the recent estimation of the MW mass distribution (e.g. [Kafle et al. 2014](#)).

The dynamical friction due to the dark matter halo is described by the Chandrasekhar equation ([Chandrasekhar 1943](#)):

$$\mathbf{F}_{\text{df}} = -\frac{4\pi G^2 M_{\text{sat}} \ln(\Lambda) \rho(\mathbf{r})}{v^2} \left[\text{erf}(X) - \frac{2X}{\sqrt{\pi}} \exp(-X^2) \right] \frac{\mathbf{v}}{v}, \quad (5)$$

where $\rho(\mathbf{r})$ is the density of the MW halo, v is the orbital velocity of a satellite with mass M_{sat} . The parameter $X = c/\sqrt{2\sigma^2}$ includes the velocity dispersion of the particles in the host halo. In this paper, we follow the analytical approximation for σ for a NFW profile

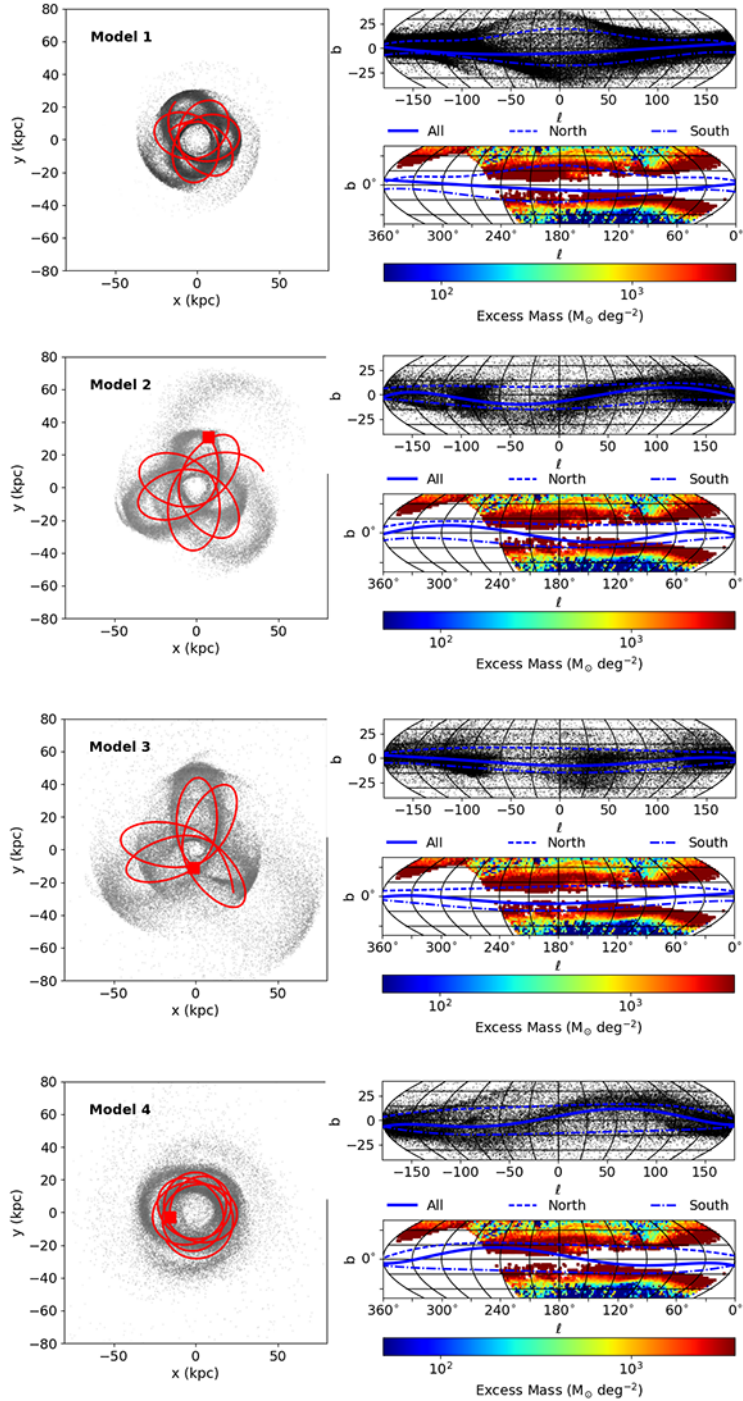


Figure 1. Results from a GA run on all three mass models (see 2). *Left panels:* Projection of particles in the (x, y) plane after 3 Gyr. The solid red lines in all plots show the orbit of the progenitor, whose present-day position is indicated by the solid red square. *Right panels:* Top: (l, b) projection of the simulated stream in the region $-40^\circ < b < 40^\circ$. The blue lines show the stream tracks for all particles (solid line), for only those particles in the northern region (dashed line) and only those in the southern region (dashed dot line). Bottom: Comparison between the particle tracks with the data as presented by Morganson et al. (2016). For the four models, the values of the fitness function are 0.98, 0.89, 0.96, 0.97 for Models 1, 2, 3 and 4 respectively.

as described by Zentner & Bullock (2003). The parameter $\ln(\Lambda)$ is the Coulomb logarithm and Λ is defined here as the ratio between the radial position of the satellite and the impact parameter. This is chosen to be 2.0 kpc for Model 1, 2.5 kpc for Model 2 and 3.5 kpc for Model 3 and 4.

The influence of dynamical friction on the satellite orbits depends on the satellite mass and its velocity, two unknowns in our simulations. To overcome the lack of information on the mass, we have used three different mass models for the satellite as indicated in Table 2. Early results, based on the Sloan Digital Sky Survey,

Model	$M_{\text{DM}} (10^{10} M_{\odot})$	$M_{*} (10^{10} M_{\odot})$
Model 1	0.03	0.003
Model 2	0.88	0.04
Model 3	1.13	0.05
Model 4	1.57	0.60

Table 2. Satellite Mass Models for Initial Conditions.

suggested that the total stellar mass in the Monoceros Ring is between $2 \times 10^8 M_{\odot}$ and $\sim 10^9 M_{\odot}$ (Ibata et al. 2003). Based on Pan-STARRS data, Morganson et al. (2016) estimate a total mass for the Monoceros ring in the range $[4, 6] \times 10^7 M_{\odot}$. The stellar mass models used in our simulation span from 2×10^8 to $1 \times 10^9 M_{\odot}$. The dark matter halo mass changes according to the stellar mass, so that the baryonic fraction (stellar mass over dark matter mass) is approximately 0.07 in all models.

2.2 Genetic Algorithm: Parameter Space and Orbit Selection

Genetic Algorithms (GAs) are powerful population-based algorithms, able to solve optimisation problems by mimicking biological evolution. Starting from an initial *population* of possible solutions (*individuals*), the algorithm identifies those that better satisfy the model requirement. Each individual corresponds to a combination of free parameters, whose fitness depends upon the value of a merit function that describes the problem to convey. The best, or ‘fittest’, individuals are then used to generate a new set of solutions to form the next generation. At each step, the population evolves toward an optimal solution.

Free parameters in our GA are the past position and velocity of the progenitor, and they correspond to the only parameters used to identify the best orbital model. The (x, y, z) positions are randomly selected between -50 kpc and 50 kpc from the Galactic Centre. The corresponding components of the total velocity are selected in such a way that 3 Gyr ago the satellite was gravitationally bound to the Milky Way, or rather, that its total velocity was less than the MW escape velocity at that position. Within the (x, y, z) range defined above the GA randomly selects (vx, vy, vz) between -230 and 230 km s^{-1} .

Our populations consist of 50 possible solutions, each corresponding to particular initial conditions that are passed to the N -body code. After 3 Gyr, the present day simulated snapshot is compared to observations. This comparison is done by firstly checking for the presence of stream-like structures. We define a ‘stream’ as an over-dense structure of baryonic particles not gravitationally bound to the progenitor. The code selects all particles initially associated with the satellite stellar component and estimates the density of each based on the nearest particles. Stream candidates are those particles with a density greater than the total mean density.

If the simulation produces a stream, the code checks if it lies within the Monoceros Ring region. Morganson et al. (2016) characterised the MRI as extending from $90^\circ < l < 270^\circ$ with Northern ($3^\circ \lesssim b \lesssim 45^\circ$) and Southern ($-45^\circ \lesssim b \lesssim -3^\circ$) components. Therefore, we require that the simulated streams cover a similar range of l and present the characteristic Northern/Southern components. To do this the code considers the two components individually by creating a north and south distribution of particle positions in (l, b) . For each it calculates the interquartile range (IQR_{sim}), as an indicator of the actual extent of the structure. IQR_{sim} is then compared with the equivalent value obtained from the data. These are taken

Model	M_N	M_S	$M_{*f}(r < 3 \text{ kpc})$
Model 1	$(0.03 \pm 0.01) \times 10^8 M_{\odot}$	$(0.04 \pm 0.01) \times 10^8 M_{\odot}$	-
Model 2	$(0.8 \pm 0.2) \times 10^8 M_{\odot}$	$(1.1 \pm 0.3) \times 10^8 M_{\odot}$	$(0.3 \pm 0.3) \times 10^8 M_{\odot}$
Model 3	$(1.5 \pm 0.5) \times 10^8 M_{\odot}$	$(1.2 \pm 0.4) \times 10^8 M_{\odot}$	$(0.3 \pm 0.5) \times 10^8 M_{\odot}$
Model 4	$(1.7 \pm 0.8) \times 10^8 M_{\odot}$	$(1.2 \pm 0.4) \times 10^8 M_{\odot}$	$(0.5 \pm 0.3) \times 10^8 M_{\odot}$

Table 3. This table lists the distribution of the stream mass in the Northern and South component; the progenitor final stellar mass distribution. The latter indicates the stellar mass within 3 kpc from the satellite centre (the lowest mass progenitor, Model 1, is totally destructed by the interaction with the Galaxy). The distributions are obtained by considering a sample of 1000 GA possible solutions with fitness function > 0.9 (see text for more details). For all the four mass models, the results for the stream Northern and Southern components are not consistent with the mass given by Morganson et al. (2016). From observations, the Northern and Southern component have mass around $6 - 8 \times 10^6 M_{\odot}$ and $4 - 5 \times 10^7 M_{\odot}$ respectively, while our simulations show a mass of a factor of ten time higher than the expected value. (See text for more details)

from the density map presented by Morganson et al. (2016) but focusing only on pixels with more than $100 M_{\odot}$ excess mass. Each component is then compared with the data via:

$$F_{N,S} = \frac{1.0}{1.0 + \left(\frac{(\text{IQR}_{\text{sim}})_{N,S} - (\text{IQR}_{\text{data}})_{N,S}}{\sigma_l} \right)^2} \quad (6)$$

$$+ \frac{1.0}{1.0 + \left(\frac{(\text{IQR}_{\text{sim}})_{b_{N,S}} - (\text{IQR}_{\text{data}})_{b_{N,S}}}{\sigma_b} \right)^2} \quad (7)$$

where $(\text{IQR}_{\text{data}})_N = 164.0^\circ$, $(\text{IQR}_{\text{data}})_S = 141.0^\circ$, $\sigma_l = 20^\circ$, $(\text{IQR}_{\text{data}})_{b_N} = 28.0^\circ$, $(\text{IQR}_{\text{data}})_{b_S} = -20.0^\circ$, both with $\sigma_b = 10^\circ$. The choice of σ_l and σ_b is arbitrary and used only to define a degree of similarity between the data and simulation. The final fitness function is defined as the product of each component:

$$F = F_N * F_S \quad (8)$$

and it is normalised to be 1 for a perfect match with observations.

No further conditions are set for structures outside the defined region of the two components or on the orbit of the satellite. Optimal orbits are chosen based on the value for the fitness function (Equation 8).

3 RESULTS

For each mass model in Table 2, we study the evolution of an initial population of 50 individuals for a maximum of 50 generations. For each individual in the population, we study the interaction between the satellite and the MW for 3 Gyr, starting from the past position randomly chosen by the GA as described in the previous section. The final snapshot corresponds to the present day position and it is used to evaluate the fitness function (Equation 8).

Figure 1 shows an example of best solutions found by the GA for each mass model in Table 2. The specific mass models are indicated in the panels. The figure includes the final particle positions in the (x, y) projection (left panels), with the progenitor orbits plotted as a red solid line. The left panels show the (l, b) projection of the simulated streams in the Monoceros region ($-40^\circ < b < 40^\circ$). In the top panels, the *black points* show the particle distribution in (l, b) as a result of the 3 Gyr interaction, while the *blue lines* show the average track of the stream for the Northern (*dashed blue line*)

and the Southern (*dashed dot blue lines*) components and the for the entire stream (*solid blue lines*). In the bottom panels, the same line tracks are compared with the Pan-STARRS density (Morganson et al. 2016). As in Morganson et al., the map describes the total excess mass along the line of sight and it directly compares to their Figure 12.

As shown Figure 1, the (l, b) projections of each GA run produce well-defined Northern and Southern structures similar to those observed in the Pan-STARRS data. These models have fitness values greater than ~ 0.89 , indicating that they reproduce the observed extent of the stream ($90^\circ < l < 270^\circ$) in the north ($3^\circ \lesssim b \lesssim 45^\circ$) and south ($-45^\circ \lesssim b \lesssim -3^\circ$) fairly well.

The data presented by Morganson et al. (2016) allow for better constraints on the heliocentric distance of the MRI, showing that the southern component is closer ($d_\odot = 6$ kpc) than the northern one ($d_\odot = 9$ kpc). The models in Figure 1 do not reproduce the distances of the two components, all producing streams at distances of 10 kpc larger than expected. However, for Model 3 the simulations show a stream that is roughly 3 kpc closer in the South than in the North ($d_{S\odot} \sim 15$ kpc and $d_{N\odot} \sim 18$ kpc).

One interesting feature of the MRI overdensity is that the southern component appears to be more massive than its northern counterpart. Morganson et al. (2016) quote a mass for the Southern stream to be $4.8 \times 10^7 M_\odot$ and $8.6 \times 10^6 M_\odot$ for the Northern component. These are based on the assumption that the MRI is a uniform circle with a distance of 13 kpc and 10 kpc for the southern and northern stream respectively. The authors also note that the MRI centre (assuming a circular ring) might be off-centre by 4 kpc with respect to the Galactic centre. This change in geometry led to a 30% difference in the mass estimation, ($M_S = 3.3 \times 10^7 M_\odot$ and $M_N = 6.0 \times 10^6 M_\odot$). However, despite the change of the system geometry, the general conclusion is that the stream is more massive in the south.

To analyse the GA results we build a sample of 1000 possible solutions all with a fitness function greater than 0.9. For each solution we estimate the mass of each component as well as the stellar mass of the progenitor within a radius of 3 kpc from its centre. Among the four models, only the progenitor with mass $3 \times 10^8 M_\odot$, (Model 1), does not survive the 3 Gyr interaction with the Milky Way. In Table 3, we summarise the results of our statistical analysis indicating the mass value for the Northern and Southern components (column one and two, respectively) and the stellar mass of the progenitor remnant when possible.

In general the simulations tend to overestimate the mass of the stream components resulting in a total mass of at least ten times higher than the value suggested by observations. The overestimation is more pronounced for Model 2 and Model 3 than Model 1, for which the progenitor has a lower initial stellar mass (see Table 2). Between the three mass models, Model 1 is the only one that can reproduce a Southern stream more massive than its northern counterpart.

3.1 Progenitor location

Independent of the progenitor mass and its orbit, our simulations suggest that the progenitor survived the interaction with the Galaxy, although with a consistent mass loss.

As discussed in the previous section, the last column in Table 3 lists the final stellar mass within 3 kpc of the progenitor centre of mass. The simulations suggest that the remnant galaxy has a stellar mass of the order of $10^7 M_\odot$, although these estimations have significant uncertainties.

To identify the current progenitor location, we select a sample of 1000 possible orbits in which the satellite galaxy survived after a 3 Gyr interaction with the Milky Way. These orbits are the results of repeated GA runs using all the three mass models. In each GA run, we identified and selected a variety of orbital models with fitness value greater than 0.9 to guarantee the formation of the MRI structure. The selected orbits do not necessarily correspond to the last generation, but we extend our selection to all generations. In other words, our samples contain all orbital models able to reproduce the MRI to a reasonable precision.

Figure 2 shows a density map of all the possible progenitor locations resulting from our analysis. The colour scale is such that the green/dark regions correspond to the location with higher occurrences. For Model 2 (*top panel*), the most likely region for progenitor locations spans over a large longitude range. However, it is possible to identify three main regions around $(l, b) = (14, -1)^\circ$ (with 99% probability), $(l, b) = (352, -2)^\circ$ (97% probability) and $(l, b) = (232, 2)^\circ$ (90% probability). For Model 3 (*middle panel*) the most likely region for the progenitor location appears to be around $(l, b) = (11, -2)^\circ$ (99%) and $(l, b) = (354, -1)^\circ$ (97%). Similarly for the more massive model, Model 4 (*bottom panel*), the progenitor remnant seems to be confined in three region with comparable probability: $(l, b) = (17, -2)^\circ$ (99%), $(l, b) = (249, -1)^\circ$ (98%) and $(l, b) = (271, 2)^\circ$ (93%). By comparing the three maps in Figure 2, it is interesting that all the three models indicate the region around $(l, b) \sim (15, 0)^\circ$ as the best candidate for the progenitor location.

Figure 3 shows the distribution of the heliocentric distances for Model 2 (*blue solid line*) Model 3 (*red dashed line*) and Model 4 (*black dotted line*). As for the location in Galactic coordinates, it is difficult to constrain the distance of the progenitor due to the large scatter of its final location. However, the three distributions have similar mean values of 27 ± 12 kpc, 40 ± 12 kpc and 31 ± 13 kpc for Models 2, 3 and 4, respectively.

3.2 Stream Kinematics

In this section we analyse the kinematic distribution for the three orbital scenarios described in Figure 1. Figures 4 and 5 together describe the kinematic properties of the simulated stream for each mass model used in this work.

Figure 4 describes the heliocentric radial velocity of the stream particles. We compare our simulations (*grey points*) with the observational data by Crane et al. (2003) (*red squares*) and (Rocha-Pinto et al. 2003) (*blue triangles*), both based on the Two Micron All Sky Survey (2MASS) database. It is clear from this figure that the models well match the gradient of the radial velocity curve seen in the data, regardless the initial mass used for the satellite or its orbits. This is not surprising as different authors have shown that models with different orbital parameters, such as eccentricities or rotational sense of motion, can reproduce the observed radial velocity (Martin et al. 2004; Peñarrubia et al. 2005).

A more complete picture of the kinematic properties of the stream is provided by the proper motions of the stars in the MRI. In Figure 5, we show the latitudinal (*left panels*) and longitudinal (*right panels*) the proper motion components of all particles in the system as function of their latitude. In each panel, the proper motions of all particles in the MRI region ($90^\circ < l < 240^\circ$) are compared with those of ten confirmed stellar members (*blue squares*) presented in Peñarrubia et al. (2005) (see their Table 2). The *solid red triangles* show the stellar proper motion of the MRI obtained by combining SDSS astrometry and positions from *Gaia* DR1 (de

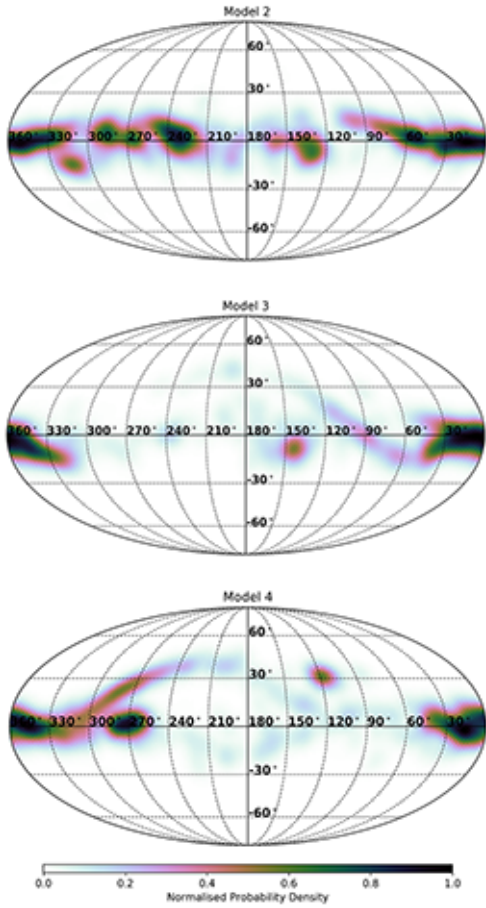


Figure 2. Mollweide Projection Map of all the possible progenitor locations in Galactic coordinates (l, b), for Models 2, 3 and 4. A satellite with mass $\sim 10^8 M_\odot$ (Model 1) does not survive the interaction with the Galaxy, hence there is no progenitor location at the end of the simulation. We consider 1000 possible orbital scenarios in each of the GA runs where the progenitor remnant is extant at the end of the simulation (after 3 Gyr). The colour map is chosen so that darker regions represent locations of higher probability.

Boer et al. 2017). As for Figure 4, all models well reproduce within the errors the stellar proper motions.

The comparison between the observed proper motions and simulations is crucial in understanding the direction, retrograde or prograde, of the progenitor orbit. As discussed in Section 2, our selection of the best models is based only on the ability of each orbit to reproduce the spatial properties of the Monoceros Ring. Therefore, there is no preference or distinction between the orbital sense of motion. Following the definition in Peñarrubia et al. (2005), we defined a prograde orbit if the orbital inclination i is less than 90° and retrograde if i is in the range 90° and 180° . The orbital inclination i is calculated as:

$$\cos(i) = -\frac{L_z}{L} \quad (9)$$

where $L = \sqrt{L_x^2 + L_y^2 + L_z^2}$ is the total angular momentum per unit of mass. In all the models in Figure 1, the progenitor lies on a retrograde orbit, with an inclination of $\approx 160^\circ$ for all three models.

In Figure 6, we compare kinematic properties of the Model 2 retrograde orbit in Figure 5 with one of its prograde equivalent (similar fitness function). Independently from their direction of mo-

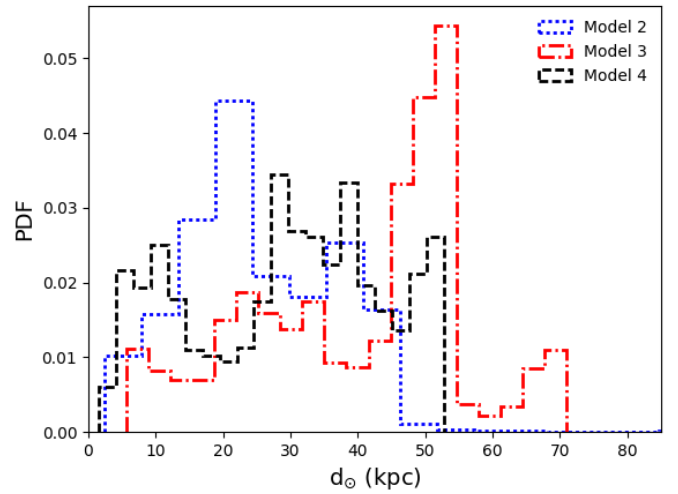


Figure 3. Distribution of the progenitor's heliocentric distance for Model 2 (red dashed line), Model 3 (black dashed line) and Model 4 (grey solid line)

tion, both models reproduce the latitudinal component of the proper motions. However, the two models produce two different ranges for the μ_l component of proper motion. In the stream region ($90^\circ \leq l \leq 240^\circ$), for the prograde orbit (right panels), μ_l spans from a minimum value of -2 mas yr^{-1} to a maximum of 0 mas yr^{-1} and for the retrograde orbit (left panels), μ_l ranges between 2 mas yr^{-1} and 5 mas yr^{-1} ², while from observations in Peñarrubia et al. (2005) $\mu_l \in (-7, 10) \text{ mas yr}^{-1}$, including a 3.5 mas yr^{-1} uncertainty. Although neither model reproduces the observed range of proper motions in full, the retrograde orbital scenario seems better encompasses the observed data points.

3.3 Comparison with data and previous models

As discussed in previous sections, Peñarrubia et al. (2005) presented the first model for the MRI, under the assumption that it formed by the disruption of an accreted satellite. The approach by Peñarrubia et al. is not dissimilar to the one presented here, as both methods used the available observational data to constrain the orbital properties of the MRI. However, the combination of a GA and N -body simulations allows us to select the optimal models through a direct comparison between simulations and observations while exploring a large parameter space. This difference implies that there are no *a priori* conditions on the orbital parameters or the progenitor orbital directions.

One of the primary results by Peñarrubia et al. (2005) is that prograde orbits are favoured over retrograde ones, as the latter fail in reproducing (in magnitude and sign) the proper motion of 10 confirmed stars members of MRI. In addition, their retrograde orbits produce a much larger azimuthal angular velocity ($\mu_l \in (5, 20) \text{ mas yr}^{-1}$) than the observations. These conclusions seem to be supported by more recent observations. Proper motion data obtained using Gaia DR1 seem to favour a prograde orbit de Boer et al.

² For the retrograde orbits, the range of the longitudinal component refers to the most dense region of the stream and ignores the more disperse particles

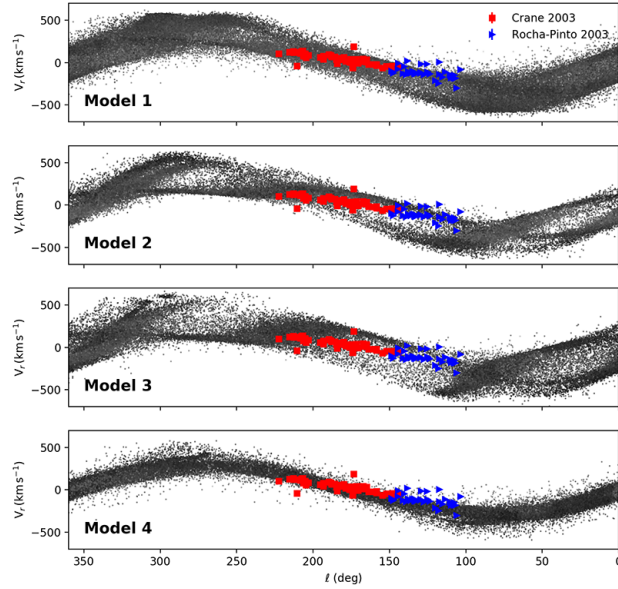


Figure 4. Heliocentric Radial Velocity versus longitude for the four models, as indicated. The radial velocities of the simulated streams are compared with the data from Crane et al. (2003) (red squares) and Rocha-Pinto et al. (2003) (blue triangles). For better comparison with observations, Sun distance and Milky Way circular velocity are 8.5 kpc and 220 km s^{-1} .

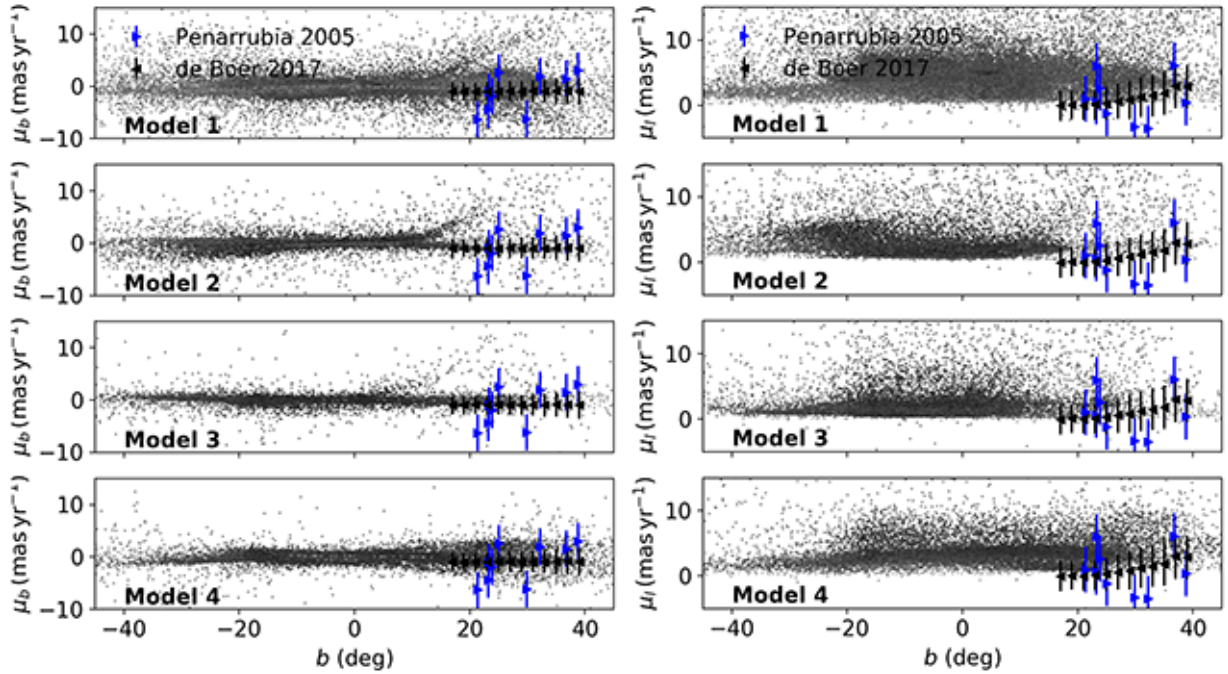


Figure 5. Proper motions in the latitudinal (left panels) and in the longitudinal (right panels) components as a function of latitude for the four mass models in Figure 1. In each panel, the blue solid triangles are the corresponding proper motion components of ten stars in the MRI identified by (Peñarrubia et al. 2005), with an error of 3.5 mas yr^{-1} . The red solid triangles show the proper motion values from Gaia DR1 as described in (de Boer et al. 2017), with error bars equal to the dispersion listed in their Table 1. For the simulated streams, the black points indicate only those particles in the region $90^\circ < l < 240^\circ$, for better comparison with observations.

(2017). On the other hand, Sheffield et al. (2014) conclude that a model with a progenitor satellite on a retrograde orbit can better reproduce the two distinct populations at the same orbital phase observed in 2MASS data.

When performing a similar analysis to the one presented by

Peñarrubia et al. (2005) (see Figures 5 and 6), our retrograde and prograde orbits can both reproduce the observed proper motion range equally. From our analysis, we conclude that it is difficult to discriminate the sign of the progenitor orbital motion from our simulations. However, it is necessary to clarify that the GA does

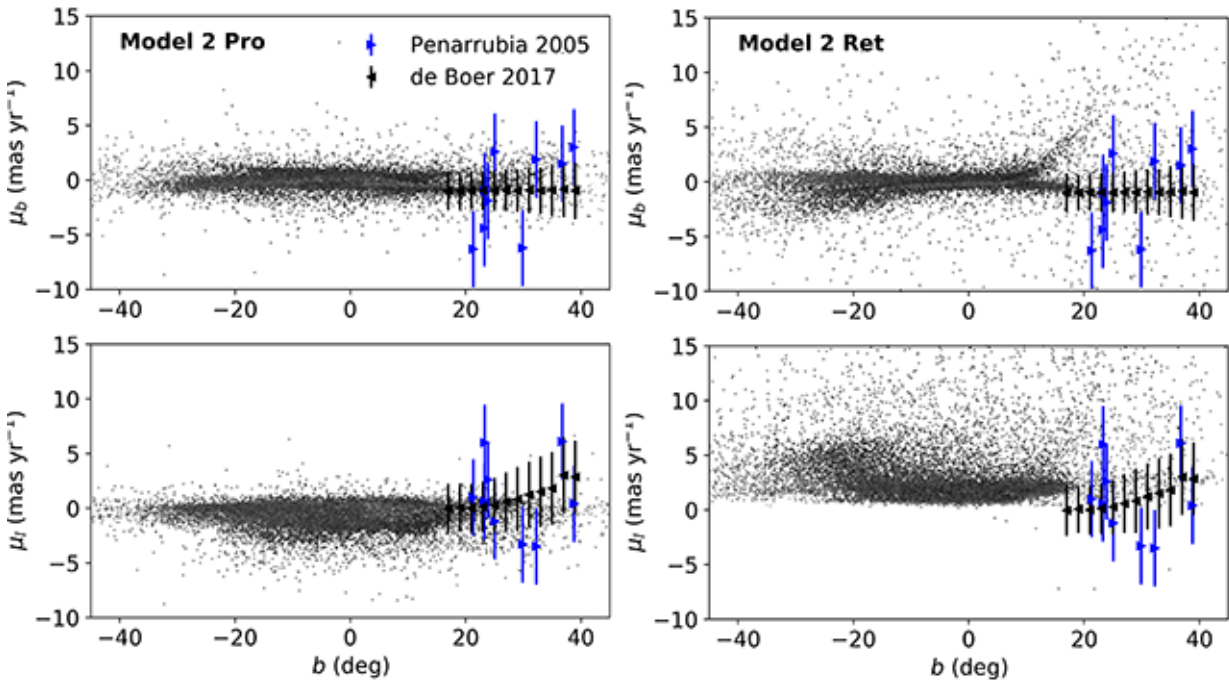


Figure 6. Comparison between retrograde (left panels) and prograde (right panels) orbit for Model 2, corresponding to a progenitor mass of $0.9 \times 10^{10} M_{\odot}$. The latitudinal (top) and longitudinal (bottom) proper motion components are compared with those by Peñarrubia et al. (2005) (blue filled triangles) and data by de Boer et al. (2017) (black filled triangles). Both orbital models reproduce the μ_b component of the proper motions well, but both fail in reproducing the μ_l data. As for Figure 5, the black points are only those particles in the region $90^\circ < l < 240^\circ$, for better comparison with observations.

not use proper motion constraints during the orbit selections. Introducing a further condition to the fitness function (Equation 7) to match the proper motions of stars in the stream will allow for a more restrictive selection of the orbital models, and hence, a better selection of the orbital sense of motion.

Due to the lack of complete and deep data sets near the Galactic plane, the estimate of the total mass of this structure poses a challenge. Using data taken with Isaac Newton Telescope Wide Field Camera, Ibata et al. (2003) predicted a total stellar mass in the structure to be between $\sim 2 \times 10^8 M_{\odot}$ and $10^9 M_{\odot}$. This estimate was based on the assumption that the MRI is smooth and axisymmetric. By interpolating across the unobserved regions in the Pan-STARRS data, Morganson et al. (2016) provide constraints on the mass of the MRI. Morganson et al. showed that the two components of the stream appear to have different masses, with the Southern overdensity ($M_S = 4 - 5 \times 10^7 M_{\odot}$) being more massive than its northern counterpart ($M_N = 6 - 9 \times 10^6 M_{\odot}$). In addition, they indicate a total mass of $10^7 M_{\odot}$ as a lower limit.

As inferred from Table 3, our models overestimate the total mass of the stream by a factor 10, and indicate equal masses for the Southern and Northern components. Only the lower mass model (Model 1) can reproduce the mass difference between the two components, albeit both of our Model 1 components have a mass smaller than the corresponding observed one.

Even considering the possibility that Morganson et al. (2016) underestimate the total mass and/or the mass of the two components, the results obtained by our Model 3 and Model 4 seem to be too high compared with observations, although the stream masses are within the limit predicted by Ibata et al. (2003) (with models giving a total stream mass of $2 - 3 \times 10^8 M_{\odot}$). On the other hand, the two models with low mass, Model 1 and Model 2, can better reproduce the mass of the two components. These results can fix

an upper limit to the mass of the progenitor to be no higher than $\approx 1 \times 10^{10} M_{\odot}$.

4 SUMMARY AND CONCLUSIONS

We have used N -body simulations in combination with a Genetic Algorithm to explore the parameter space for the initial position, orbit and final location of the progenitor to efficiently probe the possibility of an accretion origin for the Monoceros Ring. The power of this work is in the GA which allows for a best fit to the latest data and for the *first time* allows for the current location of the progenitor to be estimated, something so far lacking in the literature.

The initial location and velocity of the modelled MRI progenitor are assigned as free parameters, with the location randomly selected by the GA between -50 kpc to 50 kpc from the Galactic centre and the velocity between -230 and 230 km s $^{-1}$. The progenitor is assumed to be bound to the Galaxy after 3 Gyr of evolution using the N -body code Gadget-2 (assumed Galactic mass parameters are shown in Table 1). The fitness (Equation 8) of the final snapshot, based on comparison with PanSTARRS-1 data, is calculated.

We present here three mass models (Table 2). For Model 1 we find an MRI mass of $\sim 10^8 M_{\odot}$ and our Models 2 & 3 produce an MRI mass of $\sim 3 \times 10^8 M_{\odot}$. Morganson et al. (2016) estimate the mass to be $\sim 4 - 6 \times 10^7 M_{\odot}$. This means our models contain at least ~ 10 times the mass estimated by Morganson et al. (2016) from the Pan-STARRS dataset. This presents a problem for the accretion scenario, however, we have demonstrated, in principle, that it is possible to reproduce a Northern stream that is less massive than the Southern stream as found by Morganson et al. (2016). Even considering the possibility that Morganson et al. (2016) underestimated the total mass of the MRI and/or its two components, our

Models 2 & 3 seem to be too high. However, our modelled stream masses are within the limits predicted by Ibata et al. (2003). Because our Model 1 (the model with the lowest progenitor mass) is our only model that produced a Northern stream roughly 10 times less massive than the Southern stream we can use this to fix the upper limit of the progenitor to $\sim 10^{10} M_{\odot}$ (under the assumption that the MRI was produced via satellite accretion).

We estimate the final location of the progenitor for each of the 1000 realisations of each mass model with the results presented for our three mass models in Figure 2. For all three models we find a large range of final progenitor positions, making it very difficult to estimate a likely final position. However, it is possible to identify regions of the highest likelihood. For Model 1 we identify three regions around $(l, b) = (14, 1)^\circ$ (99% probability), $(l, b) = (352, -2)^\circ$ (97% probability) and $(l, b) = (232, 2)^\circ$ (90% probability). For Model 2 we can identify two regions at $(l, b) = (11, -2)^\circ$ (99%) and $(l, b) = (354, -1)^\circ$ (97%) and for Model 3 $(l, b) = (17, -2)^\circ$ (99%), $(l, b) = (249, -1)^\circ$ (98%) and $(l, b) = (271, 2)^\circ$ (93%). Interestingly, all three models have a high likelihood of finding the progenitor around $(l, b) \sim (15, 0)^\circ$. Similarly we find the modelled Galactocentric distances clustered around 27 ± 12 kpc, 40 ± 12 kpc and 31 ± 13 kpc for Models 1, 2 and 3, respectively. If we boldly assume that the MRI really does have an accretion origin, despite its high mass ($\sim 10^8 M_{\odot}$) the location of progenitor at $(l, b) \sim (15, 0)^\circ$ would (somewhat conveniently) make it very difficult to locate observationally due to its location behind the Bulge.

While our Model 1 gives the closest mass estimate to that by Morganson et al. (2016) and to the radial velocities by Crane et al. (2003); Rocha-Pinto et al. (2003) (Figure 4), it appears that, at least qualitatively, our Model 3 best recovers the proper motions (Figures 5 & 6). However, it should be noted that we did not include radial velocity in our GA fitting parameters so we have not done any fitting to radial velocity. Even so, the gradient of the radial velocities with Galactic longitude is well described by all three of our mass models. This shows at the very least that an accretion scenario can reproduce the observed heliocentric radial velocity profile of the MRI (as also implied by the Martin et al. 2004; Peñarrubia et al. 2005, studies).

As with the radial velocities the proper motions were not included in the fitting procedure in our models. This is further evidence that the kinematics of the MRI can be reproduced with an accretion scenario. It should be noted that in contradiction with Peñarrubia et al. (2005) the best fit models to the Pan-STARRS-1 data from all three of our mass models are all from progenitors on retrograde orbits. Those authors favoured prograde orbits in their models. Note that all of our models reproduce both the radial velocity gradient of the stream and the latitudinal component of the proper motions. However, our models produce two different ranges for the μ_l component of proper motion. In the region ($90^\circ \leq l \leq 240^\circ$), for the prograde orbit μ_l ranges from a minimum of -2 mas yr^{-1} to a maximum of 0 mas yr^{-1} and for the retrograde orbit μ_l ranges between 2 mas yr^{-1} and 5 mas yr^{-1} , while from observations $\mu_l \in (-7, 10) \text{ mas yr}^{-1}$ (including a 3.5 mas yr^{-1} uncertainty). Contrary to early models (Peñarrubia et al. 2005; Sheffield et al. 2014), we can not easily discern the favourite orbital model of the progenitor from our simulations. When compared with the observed proper motions, retrograde and prograde orbits reproduce the observations equally well (see Figure 6). However, the current version of the GA does not include any comparison between model and observed proper motions. Including such comparison in the fitness function will help in identifying the preferred orbital orientation

of the progenitor. The future data release of *Gaia* will provide crucial information on the proper motions that will offer tighter constraints on the fit that will lead to better models.

The combination of a GA and *N*-body simulations has allowed us to select the optimal models through a direct comparison between simulations and observations by exploring a large parameter space. Our models imply that there are no *a priori* conditions on the orbital parameters or the progenitor orbital directions, however, our model analyses lead to different conclusions than those presented by Peñarrubia et al. (2005) regarding the orbital direction of the progenitor.

Our models demonstrate that an accretion origin for the MRI is not excluded, but we cannot state definitively that this is the favoured scenario. Here we have explored an extragalactic/accretion origin for the MRI and, therefore, cannot discount the possibility that the observed stellar overdensity dubbed the MRI has a different origin. In a subsequent paper we will address the possibility of the rippled Disc hypothesis using a similar methodology.

ACKNOWLEDGEMENTS

RRL acknowledges support by the Chilean Ministry of Economy, Development, and Tourism's Millennium Science Initiative through grant IC120009, awarded to The Millennium Institute of Astrophysics (MAS). RRL also acknowledges support from the STFC/Newton Fund ST/M007995/1 and the CONICYT/Newton Fund DPI20140114. BCC acknowledges the support of the Australian Research Council through Discovery project DP150100862. A.Y.Q.H. was supported by a National Science Foundation Graduate Research Fellowship under Grant No. DGE-1144469. The authors acknowledge the University of Sydney HPC service at The University of Sydney for providing HPC resources that have contributed to the research results reported within this paper.

REFERENCES

- Arias, V., Guglielmo, M., Fernando, N., et al. 2016, MNRAS, 456, 1654
- Belokurov, V. 2013, New Astron. Rev., 57, 100
- Carraro, G., Vázquez, R. A., Moitinho, A., & Baume, G. 2005, ApJ, 630, L153
- Casetti-Dinescu, D. I., Carlin, J. L., Girard, T. M., et al. 2008, AJ, 135, 2013
- Chandrasekhar, S. 1943, ApJ, 97, 255
- Conn, B. C., Martin, N. F., Lewis, G. F., et al. 2005, MNRAS, 364, L13
- Conn, B. C., Lewis, G. F., Irwin, M. J., et al. 2005, MNRAS, 362, 475
- Conn, B. C., Lane, R. R., Lewis, G. F., et al. 2007, MNRAS, 376, 939
- Conn, B. C., Lane, R. R., Lewis, G. F., et al. 2008, MNRAS, 390, 1388
- Conn, B. C., Noël, N. E. D., Rix, H.-W., et al. 2012, ApJ, 754, 101
- Crane, J. D., Majewski, S. R., Rocha-Pinto, H. J., et al. 2003, ApJ, 594, L119
- de Boer, T. J. L. and Belokurov, V. and Koposov, S. E. 2017, MNRAS, (submitted)
- Duffy, L. D., & Sikivie, P. 2008, Phys. Rev. D, 78, 063508
- Gómez, F. A., Minchev, I., O'Shea, B. W., et al. 2013, MNRAS, 429, 159
- Guglielmo, M., Lewis, G. F., & Bland-Hawthorn, J. 2014, MNRAS, 444, 1759
- Hashimoto, Y., Funato, Y., & Makino, J. 2003, ApJ, 582, 196
- Helmi, A., Navarro, J. F., Meza, A., Steinmetz, M., & Eke, V. R. 2003, ApJ, 592, L25
- Hernquist, L. 1990, ApJ, 356, 359
- Ibata, R. A., Gilmore, G., & Irwin, M. J. 1994, Nature, 370, 194
- Ibata, R. A., Irwin, M. J., Lewis, G. F., Ferguson, A. M. N., & Tanvir, N. 2003, MNRAS, 340, L21

Kafle, P. R., Sharma, S., Lewis, G. F., & Bland-Hawthorn, J. 2014, *ApJ*, 794, 59

Kaiser, N., Burgett, W., Chambers, K., et al. 2010, *Proc. SPIE*, 7733, 77330E

Kalberla, P. M. W., Kerp, J., Dedes, L., & Haud, U. 2014, *ApJ*, 794, 90

Li, J., Newberg, H. J., Carlin, J. L., et al. 2012, *ApJ*, 757, 151

López-Corredoira, M., & Molgó, J. 2014, *A&A*, 567, A106

Martin, N. F., Ibata, R. A., Bellazzini, M., et al. 2004, *MNRAS*, 348, 12

Martin, N. F., Irwin, M. J., Ibata, R. A., et al. 2006, *MNRAS*, 367, L69

Martin, N. F., Ibata, R. A., & Irwin, M. 2007, *ApJ*, 668, L123

Mateu, C., Vivas, A. K., Zinn, R., Miller, L. R., & Abad, C. 2009, *AJ*, 137, 4412

McMillan, P. J. 2011, *MNRAS*, 414, 2446

Michel-Dansac, L., Abadi, M. G., Navarro, J. F., & Steinmetz, M. 2011, *MNRAS*, 414, L1

Miyamoto, M., & Nagai, R. 1975, *PASJ*, 27, 533

Morganson, E., Conn, B., Rix, H.-W., et al. 2016, *ApJ*, 825, 140

Munn, J. A., Monet, D. G., Levine, S. E., et al. 2004, *AJ*, 127, 3034

Natarajan, A., & Sikivie, P. 2007, *Phys. Rev. D*, 76, 023505

Navarro, J. F., Frenk, C. S., & White, S. D. M. 1997, *ApJ*, 490, 493

Newberg, H. J., Yanny, B., Rockosi, C., et al. 2002, *ApJ*, 569, 245

Newberg, H. J., Yanny, B., Cole, N., et al. 2007, *ApJ*, 668, 221

Peñarrubia, J., Martínez-Delgado, D., Rix, H. W., et al. 2005, *ApJ*, 626, 128

Peñarrubia, J., Benson, A. J., Martínez-Delgado, D., & Rix, H. W. 2006, *ApJ*, 645, 240

Purcell, C. W., Zentner, A. R., & Wang, M.-Y. 2012, *J. Cosmology Astropart. Phys.*, 8, 027

Rocha-Pinto, H. J., Majewski, S. R., Skrutskie, M. F., & Crane, J. D. 2003, *ApJ*, 594, L115

Sheffield, A. A., Johnston, K. V., Majewski, S. R., Damke, G., Richardson, W., Beaton, R., Rocha-Pinto, H. J. 2014, *ApJ*, 793, 62

Sikivie, P. 2003, *Physics Letters B*, 567, 1

Sollima, A., Valls-Gabaud, D., Martinez-Delgado, D., et al. 2011, *ApJ*, 730, L6

Sofue, Y., Honma, M., & Omodaka, T. 2009, *PASJ*, 61, 227

Springel, V. 2005, *MNRAS*, 364, 1105

Widrow, L. M., Pym, B., & Dubinski, J. 2008, *ApJ*, 679, 1239-1259

Xu, Y., Newberg, H. J., Carlin, J. L., et al. 2015, *ApJ*, 801, 105

Yanny, B., Newberg, H. J., Grebel, E. K., et al. 2003, *ApJ*, 588, 824

Younger, J. D., Besla, G., Cox, T. J., et al. 2008, *ApJ*, 676, L21

York, D. G., Adelman, J., Anderson, J. E., Jr., et al. 2000, *AJ*, 120, 1579

Zentner, A. R., & Bullock, J. S. 2003, *ApJ*, 598, 49

This paper has been typeset from a *TeX/LaTeX* file prepared by the author.